RESPIRATORY PHYSIOLOGY
& NEUROBIOLOGY

Relative motion of lung and chest wall promotes uniform pleural space thickness

Jean Lai [a], Andrew Gouldstone [a], James P. Butler [a], William J. Federspiel [b], Stephen H. Loring [c],*

[a] *Physiology Program, Harvard School of Public Health, Boston, MA 02115, USA*
[b] *Artificial Lung Program, University of Pittsburgh, Pittsburgh, PA 15260, USA*
[c] *Department of Anesthesia, Beth Israel Deaconess Medical Center, 330 Brookline Avenue, Boston, MA 02215, USA*

Abstract

The pleural space is modeled in two dimensions as a thin layer of fluid separating a deformable membrane and a rigid surface containing a bump. We computed the steady-state membrane configuration and fluid pressure distribution during relative sliding of the two surfaces. For physiologically relevant values of membrane tension, shear flow-induced pressures near the bump and far-field pressure gradients are similar to those measured in vivo within the pleural space (e.g. Lai-Fook et al.) [J. Appl. Physiol.: Respirat. Environ. Exercise Physiol. 56 (1984) 1633–1639]. Deformation of the membrane over the bump suggests that the pressure field generated by the sliding motion promotes an even layer of fluid in the pleural space, preventing asperities from touching. Results also suggest a possible mechanism for pleural fluid redistribution during breathing, whereby irreversible fluid motion is associated with the deformability of the membrane. © 2002 Elsevier Science B.V. All rights reserved.

Keywords: Mechanics of breathing; Pleural space thickness; Model, pleural space, fluid dynamics; Pleura, fluid, redistribution; Pressure, shear flow-induced

1. Introduction

For homogeneous expansion of lung parenchyma and effective inspiratory action of the diaphragm, the lungs and chest wall must slide against each other during breathing (Mead, 1979).

The mesothelial tissue lining the pleural space exhibits roughness on different size scales that, in the absence of sliding or other dynamic process, would lead to contact between the surfaces. Agostoni (1986) suggested that such points of contact could explain the less-than-hydrostatic pressure gradient measured in the mammalian pleural space. However, the persistence of such points of contact as the lung slides against the chest wall during breathing would produce high shear stresses, and possibly damage the mesothelial surfaces. In this paper, we describe a dynamic mech-

* Corresponding author. Tel.: +1-617-667-3092; fax: +1-617-667-1500.

E-mail address: sloring@caregroup.harvard.edu (S.H. Loring).

anism that separates sliding pleural surfaces in regions of close proximity, and thus prevents contact. Such a process serves to maintain uniform pleural space thickness and reduce shear stresses during breathing.

We approach this phenomenon through the fluid dynamics of shear flow when bounding surfaces are not parallel, but contain local unevenness. An important feature of our model, not present in other fluid dynamical studies of similar shear flow, is that the channel geometry can deform in response to pressures caused by shear flow. In particular, we consider the problem of two-dimensional (2-D) steady shear flow between a compliant membrane under tension and a rigid uneven surface. Although our study used a simple model vis-a-vis pleural geometry and deformation, the fluid mechanical description obtained, interpreted in the context of underlying mechanism, possesses clear implication for pleural fluid dynamics, as well as other problems involving shear flow within deformable channels.

2. Methods

2.1. Basic model

The model consists of a 2-D channel between two surfaces (Fig. 1). The top surface, for illustration representing a portion of visceral pleura, is a deformable membrane, while the bottom surface, similarly representing a portion of parietal pleura, is rigid. The two surfaces are planar and parallel, with a gap thickness of $h(x) = h_g$ representing the average thickness of the pleural space, except for a local region where the gap thickness varies. The Figure shows a one-dimensional Gaussian shaped

bump on the bottom surface, symmetric about the origin, whose height is given by $y = h_b \exp(-2x^2/w^2)$, where the Cartesian coordinate system (x,y) is asymptotically parallel to the channel $(y = 0)$ and w is a length scale for the bump width. These characteristic dimensions are chosen, relative to the channel, to be consistent with surface asperities shown in light micrographs of the pleural space (Albertine et al., 1991). The relative motion between lung and chest wall is represented by motion of the deformable membrane (top surface) with steady velocity U in the x-direction. In this model, we only consider steady state solutions.

2.2. Governing equations

The characteristic dimensions involved in the pleural space are microscopic ($h_g = 10$–30 μm) and for realistic velocities and kinematic viscosity of the fluid involved, the Reynolds number during pleural sliding is much less than unity. Accordingly, in this model fluid flow is governed by the Stokes equation (Panton, 1984):

$$\nabla P = \mu \nabla^2 \vec{u} \tag{1}$$

where P is pressure, μ is viscosity and $\vec{u}$ is the fluid velocity vector. The Stokes flow formulation is completed with boundary conditions on the pleural surfaces and at the two ends of the channel. No fluid slip is assumed along the pleura–liquid interfaces, and hence the velocity at the top surface is $\vec{u}_{\text{top}} = U\vec{t}$, where $\vec{t}$ is the unit tangent vector there; the velocity at the (stationary) bottom surface is $\vec{u}_{\text{bot}} = 0$. (Note that in steady state the normal velocity components on both surfaces are zero, and so filtration of fluid across these surfaces is not explicitly incorporated in the model.) Fluid flow at both ends of the channel,
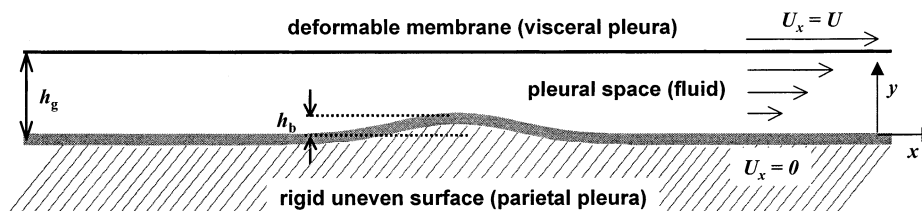

Fig. 1. A simple bump model representing local unevenness in the pleural space.

far away from the unevenness, is simple shear flow with a linear velocity profile, $(u_x, u_y) = (Uy/h_g, 0)$ (Panton, 1984), with gap thickness fixed at h_g. These boundary conditions are imposed at the (finite) ends of the channel in the computational model (Section 2.3) and asymptotically as $|x| \to \infty$ in the analytical model (Section 2.4).

The geometry of the channel is coupled to the fluid flow through the top deformable surface, which is modeled as an inextensible membrane under tension (Butler et al., 1995). Accordingly, the shape of the top surface depends on the pressure and the tension according to the membrane law:

$$P = -T\kappa \tag{2}$$

where P is fluid pressure, T is membrane tension, and $\kappa = h''/\sqrt{1 + h'^2}$ is the curvature (prime denotes differentiation with respect to x) at the top surface. When the top surface is concave upwards, $P < 0$ and when it is concave downwards, $P > 0$. Since the top surface is asymptotically flat, the pressure vanishes far away from the bump. Deformation depends only on pressure; fluid shear stresses do not directly affect the shape of the deformable membrane in this model.

2.3. Overall solution algorithm

The boundary shape of the deformable membrane depends on the pressure field through the membrane tension law, while in turn the pressure field depends on the boundary shape through the Stokes equation and associated boundary conditions. We used an iterative process to determine the simultaneous solution to these equations, by adapting the solution algorithm suggested for free-boundary problems in fluid mechanics (Ryskin and Leal, 1984). We also solved these equations in the lubrication approximation, given below in Section 2.4.

The iteration starts with the generation of a boundary-fitted computational grid to an initial geometry that consists of the prescribed unevenness on the bottom surface, and a flat, undeformed membrane on the top surface. The grid is a discrete representation of a 2-D conformal coordinate system (ξ, η) with coordinate lines coinci-

dent to all boundaries of the physical geometry (Thames et al., 1977; Thompson, et al., 1977, 1982, 1985). This allows the flow field to be efficiently determined for that geometry, assuming rigid surfaces.

The flow field is determined by recasting the 2-D Stokes flow problem from a pressure and velocity formulation to a scalar stream function ψ and scalar vorticity ω formulation (Panton, 1984), where

$$\vec{u} = \nabla \times (0,0,\psi) \tag{3}$$

$$(0, 0, \omega) = \nabla \times \vec{u} \tag{4}$$

This yields

$$\nabla^2\omega = 0, \quad \nabla\psi = \omega, \tag{5}$$

with boundary conditions following from transformation of the original velocity boundary conditions. These equations and boundary conditions are written in terms of the $(\xi\eta)$ boundary-fitted coordinates and then solved numerically on a computational grid. This is done by using finite difference approximations to differentials, and solving the simultaneous algebraic equations which arise, using the successive-over-relaxation technique (Roache, 1982).

Given the flow field for a fixed geometry, the pressure distribution over the top surface is calculated using the line integral of the Stokes equation:

$$P = \int \nabla P \cdot \vec{t}\, ds = \int \mu \nabla^2 \vec{u} \cdot \vec{t}\, ds = \int \mu \nabla \times \vec{\omega} \cdot \vec{t}\, ds. \tag{6}$$

The pressure is integrated over the top surface from a reference pressure of zero far downstream of the unevenness. The pressure distribution on the deformable membrane is then compared with the pressure required by the membrane tension law. Any imbalance is used to deform the membrane in a direction that would minimize this. The (vertical) membrane displacement, Δ, in the next iteration is given by:

$$\Delta = \alpha(P_{top} + \kappa T) \tag{7}$$

where P_{top} is the pressure at the top surface. The damping factor α attenuates the deformation of

the membrane on each iteration step avoiding instability of solutions (Ryskin and Leal, 1984). The locations of the grid points on the top surface are adjusted accordingly, and the algorithm loops back to repeat the grid generation, flow solution, and pressure imbalance check procedures.

The overall iteration is accelerated by using only a small number of intermediate iterations for the numerical grid (10) and flow field (5) in each loop after deforming the top surface. The algorithm keeps deforming the compliant surface and approximating the flow field until the steady state solution (convergence) is reached. This is determined when the pressure imbalance reflected in Δ is reduced below a fixed tolerance. After the steady state geometry and flow field are determined, the pressure throughout the fluid is computed by solving the Laplace equation for P (Panton, 1984), subject to Neumann conditions on the surface, $\vec{n} \cdot \nabla P = \vec{n} \cdot (\mu \nabla \times \vec{\omega})$, and setting pressures at the far ends of the channel to zero.

2.4. Solution for high tension membrane

The computational method outlined above becomes inefficient when membrane tension is high because the characteristic length scale for deformation of the membrane increases as $T^{1/3}$; the length of the channel required for applying the 'infinity' boundary conditions (i.e. unperturbed shear flow) becomes very large in relation to the length scale of the unevenness. Nevertheless, grid resolution on the scale of the unevenness must be maintained near the unevenness. Accordingly, we devised a hybrid technique where a full 2-D computational solution at the unevenness is combined with analytical solutions based on lubrication theory far away from the unevenness. The basis of the technique is that for high membrane tension ($T/\mu U > 100$) the compliant surface remains nearly flat even in the neighborhood of the unevenness. Conversely, far from the unevenness, on the large length scale associated with membrane deformation, the unevenness appears as a point or impulse disturbance on the bottom surface.

The deflection of the membrane is small and gradual away from the unevenness and the

Reynolds equation of lubrication hydrodynamics applies (Panton, 1984), relating the gap thickness h(x) to the pressure distribution:

$$(h^3 P')' = 6\mu U h' \tag{8}$$

The lubrication equation is coupled to the membrane law through Eq. (2), and when linearized in membrane displacement $\delta(x) = h(x) - h_g$, becomes

$$\delta''' + 8\beta^3 \delta = 0 \tag{9}$$

where $\beta = (6\mu U/T)^{1/3}/2h_g$.

The solution to Eq. (9) is a linear combination of $\exp(-2\beta x)$ and $\exp(2\beta x e^{\pm i2\pi/3})$. For an impulse disturbance at the origin, the pertinent solutions which vanish as $|x| \to \infty$ involve a single exponential decay for $x > 0$ and a damped sine and cosine for $x < 0$. The coefficients of these terms are determined by matching the deflection $\delta(x)$, and the slope $d\delta/dx$ at $x = 0$, and by relating the discontinuity in curvature $d^2\delta/dx^2$ to the pressure drop, ΔP across the impulse disturbance at the origin. The pressure difference ΔP is obtained from the full 2-D computation based on a flat membrane at the origin. In this manner the entire pressure field is known by combining the pressure fields determined by the 2-D computations in the vicinity of the unevenness with those based on lubrication theory far away from the unevenness.

3. Results

3.1. Typical results

The flow field depends on the interaction between viscous flow around the uneven rigid surface and the deformation of the bounding membrane. Accordingly, a key parameter is the dimensionless tension, $T^* = T/\mu U$, which represents the ratio of the characteristic stress required to deform the membrane to the characteristic viscous stresses. All results are displayed within the context of the model dimensions. Dimensionless pressure, curvature, distance, and membrane displacement are given by $P^* = Pw/\mu U$, $\kappa^* = wh''/\sqrt{1 + h'^2}$, $x^* = x/w$, and $\delta^* = \delta/w$, respectively, where w is the length scale of the bump width.
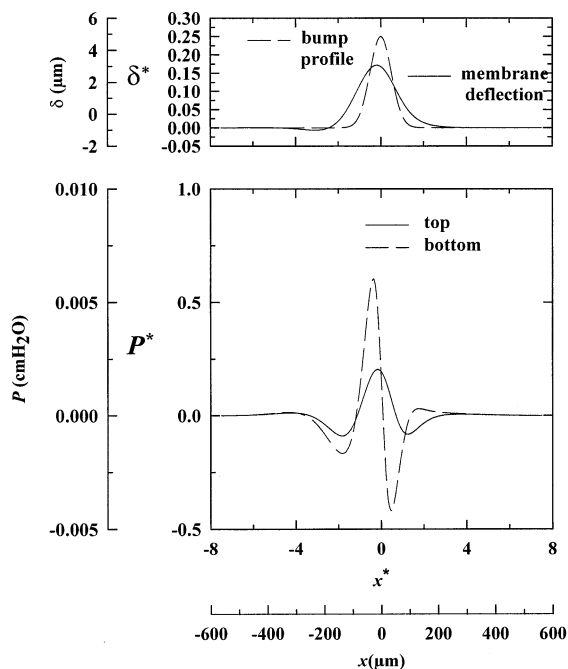
Fig. 2. For the case where the membrane and viscous force are of comparable magnitude: Top panel shows the surface deflection in relation to the bottom surface shape; Bottom panel shows pressure distribution on the top and the bottom surfaces of the model. Both the surface deflection and pressure distributions show significant deviation from reference in the neighborhood of the bump.

Results are also plotted using typical physiological values for sliding velocity, fluid viscosity and pleural space geometry ($U = 1$ cm/s, $\mu = 10^{-2}$ poise, $h_g = 20$ μm and $h_b = 5$ μm). Fig. 2 shows results obtained when the membrane and viscous forces are of comparable magnitude, ($T^* = 1$), and the gap far from the unevenness is one unit length ($h_g = w$). The top panel shows the steady state shape or displacement, $\delta(x)$, of the deformable membrane in relation to the shape of the uneven rigid surface. The membrane deforms markedly towards a shape conforming to the rigid bottom surface. Accordingly, the fluid in the channel redistributes to increase the membrane height (channel depth) near the bump. Note that the deflection of the top surface is not symmetric about the line of symmetry of the bottom bump. The maximum deflection of the top surface occurs upstream of the peak of the bump and is smaller in magnitude

than h_b. Also, the spread of the deformed membrane is greater than, but the same order of magnitude as the width of the bottom bump.

The fluid pressure distributions on the top and bottom surfaces of the channel (bottom panel) exhibit significant deviations near the bump. Upstream (left) of the bump, the bottom pressure is more positive than that on the top. The converse occurs on the downstream side of the bump. The pressures on the top surface range between $P^* = \pm 0.2$ while the pressures on the bottom surface range between $P^* = \pm 0.5$. Although pressure variations in Stokes flow can exhibit antisymmetry with respect to the mean pressure, this will be so only in domains with geometric symmetry in the direction of flow (e.g. between a rigid membrane and rigid bump) (Panton, 1984). As mentioned above, however, the membrane deforms in such a manner to destroy both the geometric symmetry of the channel and the antisymmetry of the pressure.

3.2. Effects of membrane tension

Fig. 3 displays the effects of decreasing dimensionless tension from $T^* = 1$ to 0.1, which can represent either a decrease in membrane tension, or an increase in fluid viscosity or membrane velocity. The shape, $\delta(x)$, of the deformable membrane (top panel) changes little as dimensionless tension is reduced, but the more compliant membrane shifts more to the line of symmetry of the bottom bump ($x = 0$). The pressure variation along the top surface almost vanishes for $T^* = 0.1$ (middle panel) and the pressure distribution on the bottom surface (bottom panel) approaches an antisymmetric shape about the line of symmetry of the bump. Consideration of the membrane tension law suggests that these results approximate the limit of zero tension. Although computations for smaller values of T^* were problematic, the results shown in Fig. 3 suggest that for smaller values of T^*, the pressure along the membrane would vanish, and the membrane would deform symmetrically with respect to the line of symmetry of the rigid bump. As a result, pressure variations within the channel would be perfectly antisymmetric, albeit very small.

Fig. 4 displays results for increasing dimensionless tension from a value of $T^* = 1$ to 10, 100, and 10^5. The deflection of the deformable membrane (top panel) decreases as the dimensionless tension increases and approaches zero as the tension becomes very large ($T^* = 10^5$). More importantly, the spatial spread of membrane deformation increases as T^* increases, with the maximum deflection occurring further upstream. The magnitude of the pressure variations on both bounding surfaces increases as tension increases (middle and bottom panels), and these pressure deviations occur over an increasingly larger region. In addition, the difference between pressures on the top and bottom surfaces decreases as T^* increases.

A key observation in both the deflection of the membrane and the pressure deviations shown

Fig. 4. Effect of increasing dimensionless tension T^* from 1 to 10^5. Top panel shows the gradual decrease of the compliant surface deviation which approaches zero as the tension increases. Middle and bottom panels show a nonlinear increase of the pressure as the dimensionless tension increases. Also, the region of the pressure deviation from the reference pressure increases as the dimensionless tension increases.
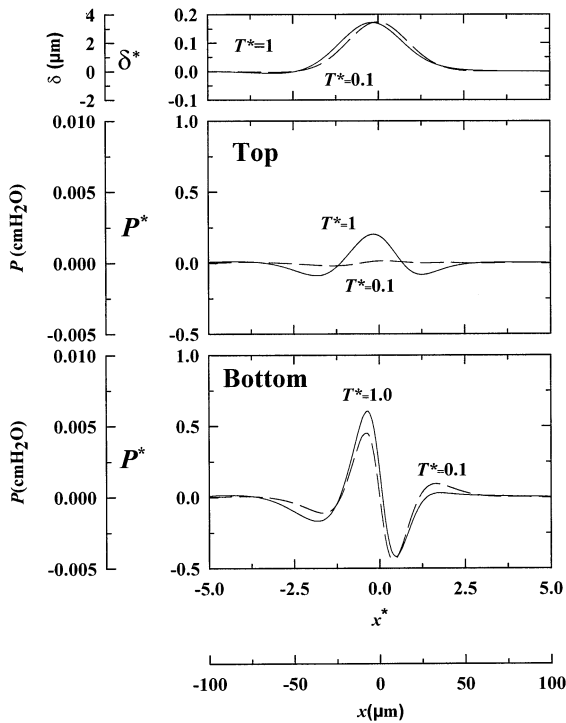

Fig. 3. Effect of decreasing dimensionless tension T^* from 1 to 0.1. Top panel shows little change in the change of the compliant surface deflection. Middle panel shows that the pressure deviation along the top surface almost disappears when $T^* = 0.1$. Bottom panel shows the pressure distribution for lower tension is closer to antisymmetric around the line of symmetry of the bump.
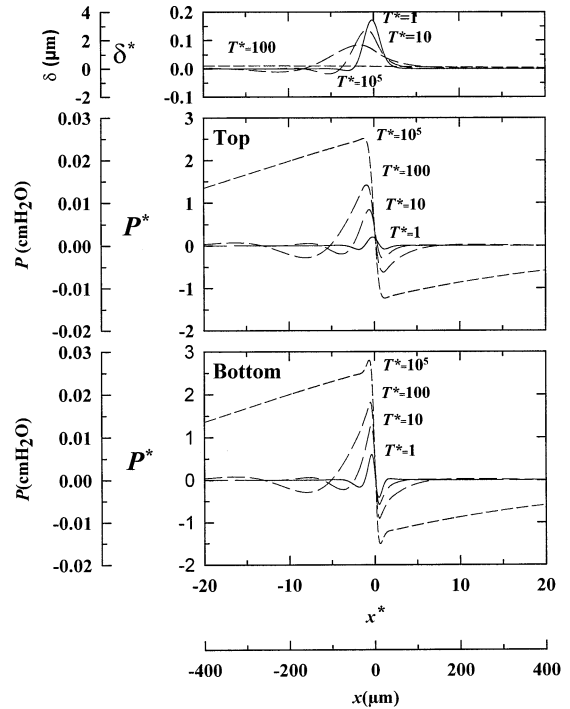
above is that the spread (in the x-direction) of these values increases with T^*. This appears to be qualitatively consistent with behavior predicted by lubrication theory. The lubrication theory solution for an impulse bump at the origin indicates damped sinusoidal variations in deflection and pressure upstream of the disturbance and pure exponential decay downstream. Furthermore, the characteristic length scale of these behaviors varies with $(T^*)^{1/3}$. Accordingly, we looked specifically at the deflection of deformable membrane $\delta(x)$, normalized by the maximum deflection δ_{max}, as a function of axial distance x for $T^* = 0.1$, 1.0, 10, and 100 (Fig. 5, top panel). Normalized membrane deflection indeed exhibits damped sinusoidal behavior upstream ($x < 0$) and exponential decay downstream ($x > 0$) of the bump. Further-

more, the location of peak deflection shifts upstream with increasing T*. As a consistent index of the extent of the deflection we computed, for each tension shown, the axial distance required for the normalized δ(x) to decrease from 0.6 to 0.1 of bump height on the downstream side. (This criterion focuses most on the pure exponential part of the response.) This length, denoted as L_d, varies almost linearly with $(T^*)^{1/3}$ (Fig. 5, bottom panel) in the range of T* from 0.1 to 100, which supports the specific predictions based on lubrication theory. Since the spread of membrane deflection varies as $(T^*)^{1/3}$ so will the extent of deviation in pressure from reference. These results highlight the fact that the deformability of the membrane affects the length scale over which the deviations from pure shear flow caused by a surface unevenness can extend beyond the unevenness.
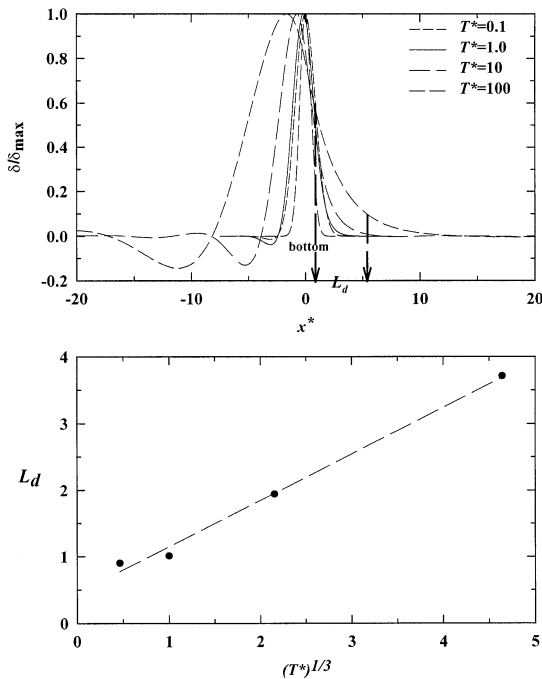

Fig. 5. Top panel shows that the compliant membrane deflection δ(x) is characterized by a damped sinusoid upstream of the bump and a exponential decay downstream of the bump. L_d, defined as the axial distance x by which normalized δ(x) decreases from 0.6 to 0.1, is an index representing the spread of membrane deviation. Bottom panel shows that L_d varies almost linearly with $T^{*\frac{1}{3}}$. Above observations are consistent with the behavior predicted by lubrication theory.
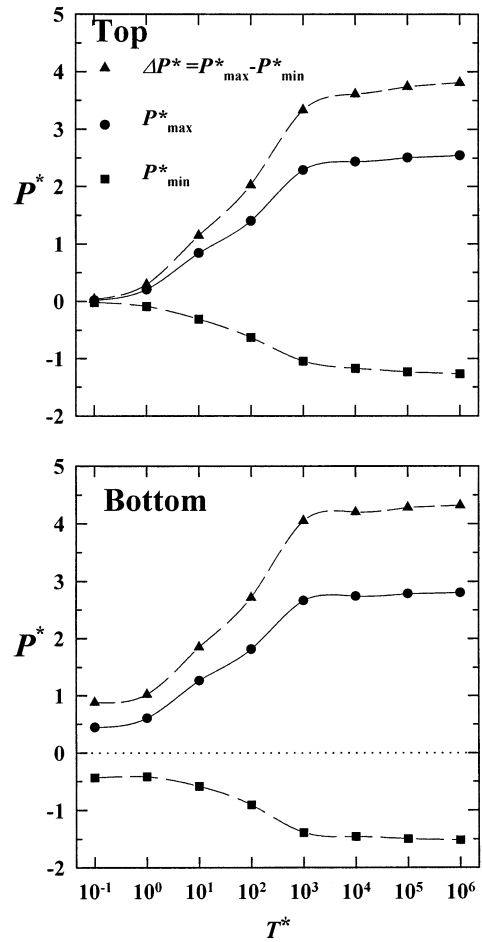

Fig. 6. The behavior of maximum pressure P^*_{max}, minimum pressure P^*_{min}, and their differences as the dimensionless tension increases. They approach plateaus when T* is either very large or very small.

The magnitude of the pressure variations associated with flow past an unevenness also exhibits interesting behavior with changes in dimensionless tension, as shown in Fig. 6. On both the top and the bottom surfaces of the channel, maximum pressure P^*_{max}, minimum pressure P^*_{min}, and their difference ΔP* are shown as a function of T* over a range from 0.1 to 10^6. The maximum and minimum pressures each approach asymptotic values on both surfaces for both large ($T^* > 10^4$) and small ($T^* < 1$) dimensionless tensions. The large T* asymptotes correspond to the respective

pressures associated with a rigid (nondeforming) top surface. Conversely, the small T^* asymptotes on the top surface (deformable surface) are zero, consistent with the membrane tension law in the limit of zero tension.

3.3. Comparison with 3-D geometry

Results from the model presented in this paper were compared with those obtained from analytical fluid dynamics simulations of unidirectional sliding of a rigid flat surface over an axisymmetric bump (Fig. 7, top panel) with pressure set to zero far away from the bump. It was found that the pressures created from sliding over an axisymmetric Gaussian bump could be described quite accurately (within 5–10%) via the lubrication equation allowing flow in two dimensions (Panton, 1984)

$$\frac{\partial}{\partial x}\left(h^3\frac{\partial P}{\partial x}\right) + \frac{\partial}{\partial z}\left(h^3\frac{\partial P}{\partial z}\right) = 6\mu U\frac{\partial h}{\partial x} \qquad (10)$$
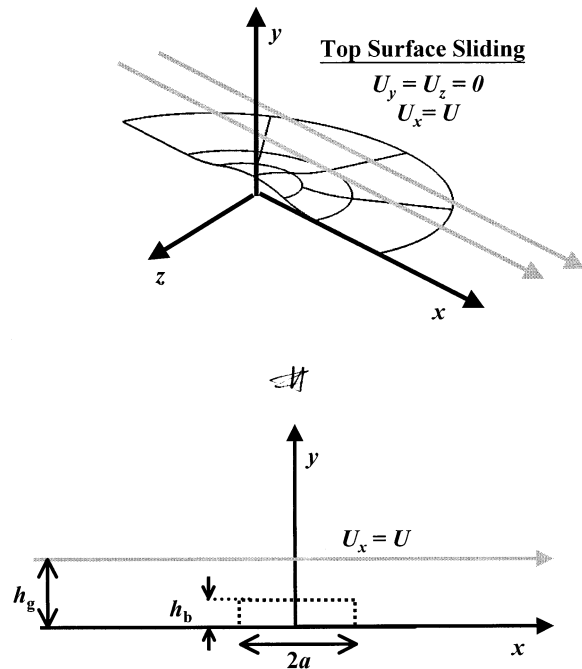

Fig. 7. Top panel displays a schematic of unidirectional sliding over an axisymmetric Gaussian bump. Bottom panel displays the approximation of a Gaussian bump as a cylinder of radius a and height h_b.

applied to a situation in which a flat plate slides over a cylindrical bump of height h_b and radius a (cross section shown in Fig. 7, bottom panel), which is approximately equal to the width at half height of the corresponding Gaussian bump. The pressure along the x-axis is given by

$$P = \frac{6\mu Uh_b}{h_g^3 + (h_g - h_b)^3} \times \begin{cases} x, & x \le a \\ a^2/x, & a \le x \end{cases} \qquad (11)$$

This result was confirmed with full 3-D computational simulations (ADINA-F, Watertown MA, USA).

4. Discussion

4.1. Physiological pressures

The physiological relevance of the results presented here depends on the degree to which the pressures generated by shear flow deform the surrounding tissues, i.e. on the elastic moduli of the pleural tissues and lung. Quasi-static punch indentation experiments on pleurae and lung parenchyma have shown Young's modulus E of such materials to be 10^3–10^4 dynes/cm^2 (Lai-Fook et al., 1976; Hajji, 1978; Hajji et al., 1979; Stamenovic, 1984). The appropriate value for equivalent membrane tension is given by Ew, where w is the punch width, typically on the order of 1 cm. This results in equivalent membrane tensions of 10^3–10^4 dynes/cm. Deformations of the pleural membrane and underlying lung parenchyma therefore correspond in our model to a relatively stiff membrane with a dimensionless tension T^* of 10^5–10^6 (for U = 1 cm/s and $\mu = 10^{-2}$ poise).

In a review of studies on parenchyma (Fredberg and Stamenovic, 1989), it was established that lung tissue does not behave in such an idealized fashion; it exhibits structural damping in response to dynamic mechanical loading. Our analysis, while describing the steady state in the sense that the membrane deformation in the reference frame of the bump is shape stable, nevertheless represents a dynamic loading of the membrane with a deformation rate comparable to sliding velocity. It is likely that structural damping could therefore
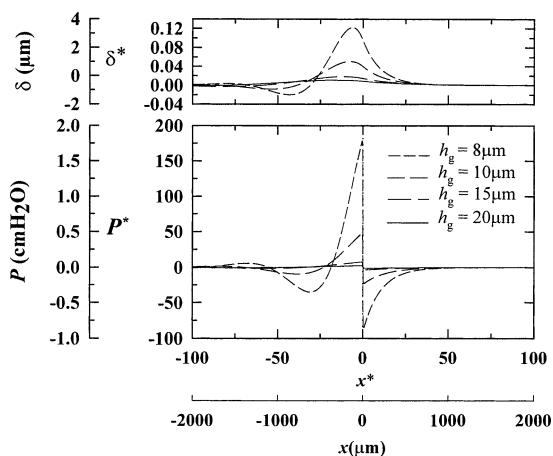
Fig. 8. For the case of realistic pleural membrane tension ($T^* = 10^5$): compliant surface deviation (top panel) and pressure distributions (bottom panel) on top surface increase very rapidly as the distance between the opposed surfaces decreases. For this value of T^*, pressures along top and bottom surfaces are equal.

affect these results, most likely by decreasing the maximum deflection of the membrane, or by broadening the downstream deflection relative to the perfectly elastic case. Whether this is quantitatively important is unknown.

For the physiological parameters described above, Fig. 8 shows the deflection $\delta(x)$ of the elastic membrane for $h_g = 20, 15, 10,$ and 8 μm, with $h_b = 5$ μm. The maximum deflection is negligible for h_g above 15 μm, but increases markedly for h_g values less than that. This suggests that for such bump geometries and membrane-like behavior of the pleural surface, contact between the two surfaces, even in the presence of asperities, is strongly resisted. The bottom panel of Fig. 8 shows the pressure distribution along the membrane surface (2-D model) for the above set of geometries. The deviation of pressure magnitude increases nonlinearly from 0.025 to 2 cmH$_2$O as h_g decreases. A pressure of 2 cmH$_2$O is comparable to the pressure causing fluid flux across the pleural membrane (Miserocchi et al., 1989). There are also two pressure gradients to consider; the gradient over the bump is rather high in all cases (5–40 cmH$_2$O/cm) but extends only 20–40 μm in the lateral direction, and the gradients upstream and downstream of the bump are between 0.1 and

1 cmH$_2$O/cm. These latter pressure gradients extend from 100 to 1000 μm away from the bump, and are the same order of magnitude as those gradients experimentally observed in the pleural space (del Fabbro, 1998; Lai-Fook et al., 1984; Wiener-Kronish et al., 1985). This result suggests that this bump configuration could have far-reaching effects on fluid redistribution in the pleural space.

By contrast, Fig. 9 displays the pressure distribution along the x-axis, in the x–y plane for the 3-D model, for gap thicknesses and physiological parameters as above. The first observation to note is the magnitude of the pressure—ranging from 0.002 to 0.05 cmH$_2$O—which is an order of magnitude lower than the 2-D result. This is not surprising, as flow is not constrained in the y-direction, allowing some fluid to flow around the bump. The second observation is the effect of decreasing h_g on pressure. As h_g is decreased from 20 to 8 μm, the magnitudes of both the maximum and minimum pressures increase by roughly 80-fold in the 2-D membrane model, but by only 20-fold in the 3-D model. There are significant pressure gradients in the vicinity of the axisymmetric bump (~ 20 cmH$_2$O/cm); however, these
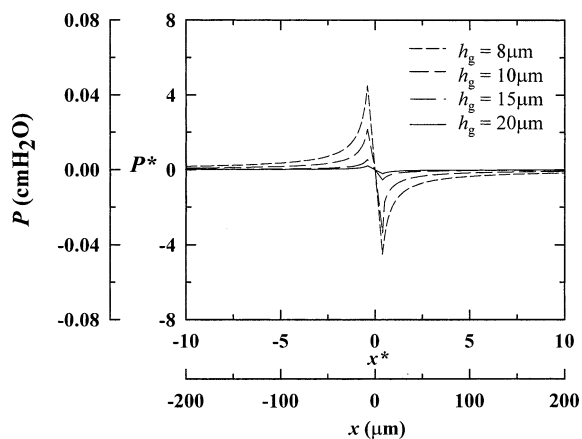

Fig. 9. Pressure in the x–y plane, along the direction of motion for a flat surface sliding over a cylindrical bump of projected width $2a \approx 10$ μm and height $h_b = 5$ μm, with physiological input parameters U (1 cm/s) and μ (10^{-2} poise). Gap thickness h_g is varied from 20 to 8 μm. Pressures (cmH$_2$O) are an order of magnitude lower than those generated with the 2-D (infinitely long) bump.

gradients are more localized than with the 2-D bump.

Deformation of the solid in the 3-D model was negligible in all cases, and is not shown here. However, deformation in such models is strongly dependent on the geometries involved, as well as tissue and fluid properties. Eq. (11) shows that maximum pressure would increase linearly with the width of the cylindrical bump, and a bump of sufficiently large radius would produce high enough pressures to significantly deform the elastic surface. Similarly, the nonlinear increase in pressure with decreasing gap thickness assures that close approximation of surfaces would generate large pressures, tending to keep the surfaces apart.

It is intuitive that a bump of width 2a and infinite length (with flow confined to the x-direction) has a more far-reaching effect on fluid flow than does an axisymmetric bump of radius a. The results presented here are consistent with this idea, and give quantitative support to the idea that nonuniformities in the bounding geometry may serve to separate pleural surfaces during shear flow. In addition, bumps shown in the membrane model could affect larger scale fluid flow, to the point that they may produce the pressure gradients observed in the pleural space.

The existence of pressure gradients associated with the relative movement of the two uneven bounding pleural surfaces implies net fluid flow within the channel. However, such motion is cyclic during breathing, and, at least in the approximate tangent planes of the pleurae, essentially reversible. This raises the interesting and important question of whether the pleural fluid flow, induced by this reciprocating motion, is also reversible. If the boundary motion is reversible in both space and time, the answer is yes (Watson, 1974). But if nonlinearities are present, the answer is no (Otani et al., 1996). Despite the strictly linear equations of motion in Stokes flow, the coupling of the boundaries, and hence the location of the boundary conditions, to the fluid pressures is sufficient to induce nonlinearities and hence irreversible flow. What remains open is the question of whether or not this irreversibility in flow, which is a necessary consequence of the pressure gradients induced by sliding motion of the lung against the chest wall, is quantitatively important to the maintenance of the pleural space.

We conclude that sliding of the pleural surfaces relative to each other is associated with fluid shear flow and the development of pressures in the vicinities of local irregularities or unevenness in gap thickness. These pressures deform the surfaces in such a way as to promote gap thickness uniformity. Furthermore, these pressures in turn will contribute to overall pleural fluid redistribution, both through transmembrane transport as well as through irreversible flow.

Acknowledgements

References

Agostoni, E., 1986. Mechanics of the Pleural Space. In: Macklem, P.T., Mead, J. (Eds.), Handbook of Physiology. Section 3: The Respiratory System, Mechanics of Breathing, Part 2, vol. III. American Physiological Society, Bethesda, MD, pp. 531–559 Chapter 30.

Albertine, K.H., Wiener-Kronish, J.P., Bastacky, J., Staub, N.C., 1991. No evidence for mesothelial cell contact across the costal pleural space of sheep. J. Appl. Physiol. 70 (1), 123–134.

Butler, J.P., Huang, J., Loring, S.H., Lai-Fook, S.J., Wang, P.M., Wilson, T.A., 1995. Model for a pump that drives circulation of pleural fluid. J. Appl. Physiol. 78 (1), 23–29.

del Fabbro, M., 1998. An improved technique for studying pleural fluid pressure and composition in rabbits. Exp. Physiol. 83, 435–448.

Fredberg, J.J., Stamenovic, D., 1989. On the imperfect elasticity of lung tissue. J. Appl. Physiol. 67 (6), 2408–2419.

Hajji, M.A., 1978. Indentation of a membrane on an elastic half space. J. Appl. Mech. 45, 320–324.

Hajji, M.A., Wilson, T.A., Lai-Fook, S.J., 1979. Improved measurements of shear modulus and pleural membrane tension of the lung. J. Appl. Physiol.: Respirat. Environ. Exercise Physiol. 47 (1), 175–181.

Lai-Fook, S.J., Wilson, T.A., Hyatt, J.R., Rodarte, R.E., 1976. Elastic constants of inflated lobes of dog lungs. J. Appl. Physiol. 40 (4), 508–513.

Lai-Fook, S.J., Beck, K.C., Southorn, P.A., 1984. Pleural liquid pressure measured by pipettes in rabbits. J. Appl. Physiol.: Respirat. Environ. Exercise Physiol. 56 (6), 1633–1639.

Mead, J., 1979. Functional significance of the area of apposition of diaphragm to rib cage. Am. Rev. Respir. Dis. (Part 2 Supplement) 119 (2), 31–32.

Miserocchi, G., Negrini, D., Mukenge, S., Turconi, P., Del Fabbro, M., 1989. Liquid drainage through the peritoneal diaphragmatic surface. J. Appl. Physiol. 66 (4), 1579–1585.

Otani, Y., Butler, J.P., Emi, H., Tsuda, A., 1996. Flow-induced mixing at low Reynolds number in an expanding and contracting alveolus model. In: Marijnissen, J.C.M., Gradon, L. (Eds.), Aerosol Inhalation: Recent Research Frontiers. Kluwer Academic Publishers, The Netherlands.

Panton, R.L., 1984. Incompressible Flow. Wiley, Toronto chapter 6 and 21.

Roache, P.J., 1982. Computational Fluid Dynamics. Hermosa Publishers, Albuquerque chapter 3.

Ryskin, G., Leal, L.G., 1984. Numerical solution of free-boundary problems in fluid mechanics. Part 1. The finite-difference technique. J. Fluid Mech. 148, 1–17.

Stamenovic, D., 1984. Mechanical properties of pleural membrane. J. Appl. Physiol.: Respirat. Environ. Exercise Physiol. 57 (4), 1189–1194.

Thames, F.C., Thompson, J.F., Mastin, C.W., Walker, R.L., 1977. Numerical solution for viscous and potential flow about arbitrary two-dimensional bodies using body-fitted coordinate systems. J. Comp. Phys. 24, 265–273.

Thompson, J.F., Thames, F.C., Mastin, C.W., 1977. Boundary-fitted Curvilinear Coordinate Systems for Solution of Partial Differential Equations on Fields Containing any Arbitrary Two-dimensional Bodies. (NASA Contractor Report) Mississippi: Mississippi State University.

Thompson, J.F., Warsi, Z.U.A., Mastin, C.W., 1982. Boundary-fitted coordinate systems for numerical solution of partial differential equations—a review. J. Comput. Physics 47, 1–108.

Thompson, J.F., Thames, F.C., Mastin, C.W., 1985. Numerical Grid Generation. Foundation and Applications. Elsevier Science Publishing, New York, pp. 1–91 chapter 1, 2.

Watson, E.J., 1974. Fluid flow in a model alveolar sac (Appendix). J. Appl. Physiol. 37 (2), 249–251.

Wiener-Kronish, J.P., Gropper, S.J., Lai-Fook, M.A., 1985. Pleural liquid pressure in dogs measured using a rib capsule. J. Appl. Physiol. 59 (2), 597–602.